Interplay of turbulent transport and Reynolds stress in drift-wave turbulence

R. Sarkis ,[1,*] N. Dumerat ,[1] B. Schmid,[1] G. E. M. Tovar ,[1,2] and M. Ramisch [1]
[1]*Institute of Interfacial Process Engineering and Plasma Technology (IGVP), University of Stuttgart, Pfaffenwaldring 31, 70569, Stuttgart, Germany*
[2]*Fraunhofer Institute for Interfacial Engineering and Biotechnology (IGB), University of Stuttgart, Nobelstraße 12, 70569, Stuttgart, Germany*

(Received 25 October 2024; accepted 24 March 2025; published 11 April 2025)

The dynamical interplay between turbulent particle transport (Γ) and Reynolds stress ($\Re$) at the edge of toroidal magnetically confined plasmas is experimentally investigated on the basis of the cross-coupling between density and potential fluctuations in drift-wave turbulence. Both Γ and $\Re$ are found to be temporally anticorrelated, with a dynamical coupling of the density and potential fluctuations as an agent in their interplay. The density-potential coupling is shown for the first time to be dynamically related to the Reynolds stress in agreement with the $E \times B$ vortex-tilting mechanism. Consistently, a temporal deterioration of the coupling links the evolution of particle transport to the drop in the Reynolds stress. Small-scale contributions ($k_\theta \rho_s > 0.6$) are shown to play a key role via a mutual stabilization-destabilization process.

DOI: 10.1103/PhysRevE.111.045207

I. INTRODUCTION

Cross field turbulent particle transport (Γ) determines the losses in magnetically confined toroidal fusion plasmas [1] and thus limits the confinement quality. The transition from low to high confinement regimes provides transport control options through the spontaneous formation of transport barriers [2,3]. Turbulence-generated zonal flows, which are poloidal $E \times B$ shear flows driven by radially localized Reynolds stress ($\Re$) [4], were identified as a trigger of L-H transitions [5–9]. Energetically, $\Re$ establishes an energy transfer from small-scale fluctuations to a mesoscopic structure [10–13], which, due to its intrinsic poloidal potential homogeneity on a flux surface, does not contribute to cross field $E \times B$ particle transport [6]. Hence, zonal flows tap energy from the scales that cause particle transport, giving rise to a predator–prey-like interplay between $\Re$ and Γ.

Eddy tilting is an essential mechanism for this energy transfer [14]. Finite, nonzero Reynolds stress $\Re = \langle \tilde{v}_\theta \tilde{v}_r \rangle$ arises from an associated asymmetry in the radial-poloidal velocity distribution. The tilt can be imposed by shear in the background flow or originate from magnetic shear in magnetized plasmas [15–17]. An initial, even random shear could trigger the onset of Reynolds-stress-driven zonal flows, which are then further enhanced through a self-amplification process [18–20].

In drift-wave turbulence, the efficiency of the Reynolds-stress mechanism depends on the parallel electron dynamics. In the case of an adiabatic, that is, instantaneous, parallel electron response to a pressure perturbation, a plasma-potential perturbation evolves without delay and identically in perpendicular shape. Hence, a tilt in the potential and thus the corresponding vortex evolves in response to a tilt in the initial pressure perturbation. In numerical simulations, this adiabatic coupling between pressure and potential perturbations has turned out to be the dominant mechanism for zonal-flow formation [14]. Moreover, a reduction of the adiabatic coupling was observed to reduce zonal-flow activity [14,21].

In basic drift-fluid models with constant temperature [22,23], electron collisionality controls the adiabatic coupling between density ($\tilde{n}$) and potential ($\tilde{\phi}$) fluctuations [24]. Ideal drift-wave turbulence with adiabatic electrons exhibits a zero density-potential cross-phase. The vortex-like $E \times B$ motion follows the density perturbation contours and, hence, does not produce net turbulent particle transport $\Gamma = \langle \tilde{n} \tilde{v}_r \rangle$. A reduction in adiabaticity introduces a phase delay between density and potential perturbation. Moreover, their dynamics tend to decouple: density evolves more and more independently of vorticity and adopts its spatiotemporal behavior as being advected more passively in the flow field [23,24]. Consequently, the density decouples from the potential, favoring an increased correlation with the velocity. As a result, Γ tends to increase.

Comparing the formation mechanisms of Reynolds stress and turbulent particle transport in drift-wave turbulence, both apparently rely on opposing prerequisites: while $\Re$ requires a strong adiabatic coupling reflected in zero $\tilde{n}$-$\tilde{\phi}$ cross-phase, Γ rather manifests itself in a decoupling process with a phase delay.

Magnetic field-line curvature drives the polarization of density perturbations and adds to the phase delay of the plasma potential [25]. With respect to the magnetic flux surface, both negative normal and positive geodesic curvature can lead to drift-wave destabilization [26] and deteriorate the adiabatic $\tilde{n}$-$\tilde{\phi}$ coupling [27]. Correspondingly, an asymmetry has been found in the poloidal Γ profile, which is in agreement with linear growth rates of drift waves in toroidal

*Contact author: ralph.sarkis@igvp.uni-stuttgart.de

stellarator geometry [28]. Deviations from this ballooning-like asymmetry might arise at increasingly important temperature dynamics [29]. Even though the curvature-driven destabilization—in terms of the deteriorated $\tilde{n}$-$\tilde{\phi}$ coupling—is not beneficial for the formation of Reynolds stress, $\Re$ has been found in the low-magnetic-shear configuration of the stellarator TJ-K to poloidally peak in the same distinct spatial region as Γ [16]. Regarding the opposing prerequisites for the formation of Γ and $\Re$, their spatial coincidence raises a contradiction. It seems likely that the necessary conditions evolve dynamically for this coincidence to occur. This means that the $\tilde{n}$-$\tilde{\phi}$ coupling hypothetically undergoes a variation in time. To investigate the interplay between Γ and $\Re$, both need to be simultaneously resolved in conjunction with a representative measure for the $\tilde{n}$-$\tilde{\phi}$ coupling.

II. EXPERIMENTAL SETUP

This work presents the first simultaneous measurements of both Γ and $\Re$, enabling their temporal correlation to unravel their interplay. To this end, $\tilde{n}$ and $\tilde{\phi}$ fluctuations are measured with a poloidal probe array. Experiments were carried out at the TJ-K stellarator [30], magnetically confining low-temperature plasmas. Under the present discharge conditions of 3 kW, 2.45 GHz microwave-heated helium plasmas at a nominal neutral gas pressure of $p = 5.5$ mPa, with an average magnetic field strength of $B \approx 68$ mT on the magnetic axis, the resulting edge electron temperature and line-averaged density are $T_e = 12$ eV and $\bar{n}_e \approx 1.4 \times 10^{17}\,\mathrm{m}^{-3}$, respectively, while ions are cold ($T_i < 1$ eV) [31]. The dynamics of TJ-K plasmas is governed by drift-wave turbulence [32,33]. In terms of dimensionless parameters ($\beta^* = 0.36$ and $\nu^* = 0.32$), it is comparable to the edge of fusion plasmas [34,35].

Figure 1 shows the array used, consisting of 128 Langmuir probes, equally distributed on four flux surfaces of a triangular cross section with a radial distance of $\Delta_r = 0.5$ cm, a poloidal probe distance of $\Delta_\theta \approx 1.5$ cm, and a probe length of 2 mm. Probe spacing is on the order of the drift scale $\rho_s = \sqrt{m_i T_e}/eB \approx 1$ cm, and well beyond the Debye length of $\lambda_D \approx 70\,\mu$m. The array data are acquired simultaneously for a period of 1049 ms, with a 1 MHz sampling rate, individually measuring either ion-saturation current ($\tilde{I}_{\mathrm{sat}}$) or floating-potential ($\tilde{\phi}_{\mathrm{f}}$) fluctuations, as indicated in the scheme of the probe arrangement in Fig. 1. Due to negligible fluctuations in T_e, the density and plasma-potential fluctuations can be taken as proportional to fluctuations in ion-saturation current ($\tilde{n} \sim \tilde{I}_{\mathrm{sat}}$) and floating potential ($\tilde{\phi}_{\mathrm{p}} \sim \tilde{\phi}_{\mathrm{f}}$), respectively [36]. The operational mode of the individual probes allows simultaneous measurement of radial turbulent particle transport on the first and fourth flux surface, together with the Reynolds stress on the second and third flux surfaces. Local estimates are obtained from measurements of the electric field for the corresponding $E \times B$ velocity components from differences in the measured potentials. With indices i and j locating the radial and poloidal position, respectively, the local particle flux is approximated via

$$\Gamma_{\mathrm{loc}}(t) = \tilde{n}(t)\tilde{v}_r(t) = \tilde{n}(t)\frac{\tilde{E}_\theta(t)}{B} \propto \tilde{I}_{\mathrm{sat},i,j}(t)\frac{-(\tilde{\phi}_{i,j+1}(t) - \tilde{\phi}_{i,j-1}(t))}{B_{i,j}\Delta_{\theta,i,j}}. \quad (1)$$

For specifying Γ in physical units, $I_{\mathrm{sat}} \sim n\sqrt{T_e}$ is employed and radial profiles of $I_{\mathrm{sat}}(R)/\sqrt{T_e(R)}$ are normalized to the line-averaged density as obtained from interferometry. Similarly, the local Reynolds stress is estimated according to

$$\Re_{\mathrm{loc}}(t) = \tilde{v}_\theta(t)\tilde{v}_r(t) = \frac{-\tilde{E}_r(t)\tilde{E}_\theta(t)}{B^2} \propto \frac{(\tilde{\phi}_{i-1,j}(t) - \tilde{\phi}_{i+1,j}(t))(\tilde{\phi}_{i,j+1}(t) - \tilde{\phi}_{i,j-1}(t))}{B_{i,j}^2\Delta_{r,i,j}\Delta_{\theta,i,j}}. \quad (2)$$

Local, individual probe spacing ($\Delta_{r,\theta}$) and magnetic-field strengths (B) from numerical computation are used for the calculation of Γ and $\Re$. A pessimistic error estimate, based on a 2-mm poloidal and radial probe misalignment, contributes by about 7% and 20% to the measured $\tilde{v}_r$ and $\tilde{v}_\theta$, respectively. An additional systematic error of 10% in the measurement of $\tilde{I}_{\mathrm{sat}}$ is used in the estimate of Γ.

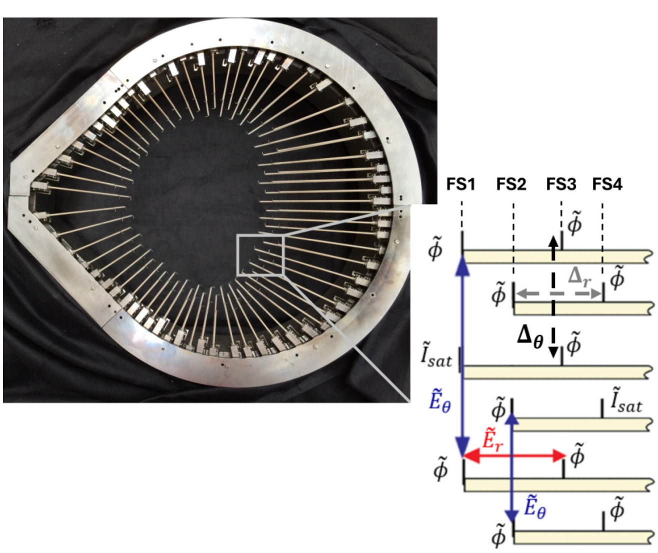

FIG. 1. Poloidal Langmuir probe array and the probes' biasing scheme allowing for the measurement of Γ on flux surfaces 1 and 4, and $\Re$ on flux surfaces 2 and 3.

III. POLOIDAL DEPENDENCE OF THE TURBULENCE

First, the poloidal profiles of the time-averaged local particle transport and Reynolds stress, as measured simultaneously, are shown in Fig. 2(a) for comparison. The shaded areas enclose the profile values between the radially separated measurement positions. Both, Γ and $\Re$ reveal their largest contribution in the same poloidal region, between 0 and $0.5\,\pi$, as was observed in previous individual measurements [16,28]. Figure 2(c) highlights that the region of local maxima is characterized by a negative normal and positive geodesic magnetic field curvature ($\kappa_n < 0$, $\kappa_g > 0$). As can be seen in Fig. 2(b), density and potential fluctuation levels show characteristics of drift-wave turbulence with comparable values. Their poloidal profile shows qualitative similarity to the distribution of Γ, exhibiting values around 25%. With a poloidal $E \times B$ shearing rate of 10 kHz over a radial probe distance Δ_r, it would take

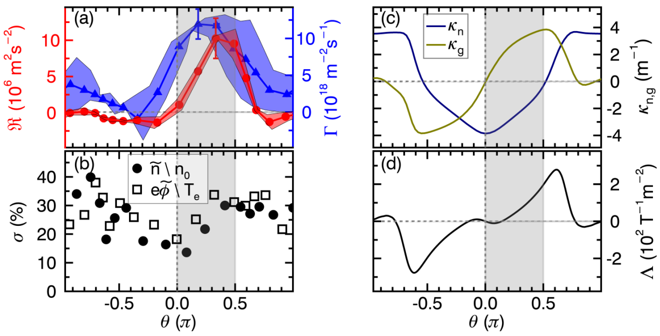

FIG. 2. Poloidal profile of (a) Reynolds stress (red, ●) and particle transport (blue, ▲) measured with the probe array, (b) the fluctuation level of density and potential, (c) the magnetic fields' normal (blue) and geodesic (green) curvature, and (d) the integrated local (Λ) magnetic shear.

600 μs for a poloidal displacement, which is observed for the peak Γ with respect to the midplane. As can be seen in the next section, the typical lifetimes of turbulent structures are much too short for the shear effect to explain the poloidal asymmetry. The asymmetry is likely due to a contribution of the positive geodesic curvature. Following an estimate of local maximum linear growth rates for drift-wave instabilities [26], regions with these curvature characteristics have the most destabilizing capacities [37]. Of all relevant terms $\sim -\kappa_n$ (symmetric), $\sim\Lambda\kappa_g$ (symmetric), and $\sim\Theta_k\kappa_g$ (asymmetric), only the last term adds to a poloidal shift. Here, Λ is the integrated local magnetic shear and Θ_k reflects the relative weight of the radial wave number in the perpendicular propagation of drift waves. Larger Θ_k are concomitant with a stronger shift within the positive κ_g frame, which is particularly characteristic of tilted vortices, also making the shift in $\Re$ plausible. A clear link between $\Re$ and magnetic shear, however, cannot be inferred from Fig. 2(d).

Following that, both $\Re$ and Γ need to be examined temporally to resolve their interplay with reference to the local competition between the adiabatic $\tilde{n}$-$\tilde{\phi}$ coupling and destabilization, as described in the introduction.

IV. TEMPORAL EVOLUTION AND INTERPLAY OF THE TURBULENT FLUXES

Net particle transport and Reynolds stress are governed by the elevated local contributions. Hence, their systematic coupling is best captured on the basis of their time-dependent poloidal averages. Moreover, this allows us to subsequently address their interplay on separated scales in poloidal wavenumber space. The coherent coupling of net Γ and $\Re$ is then obtained from conditionally sampling with respect to each other. Nonoverlapping time windows $[t_c - \tau/2\ ,\ t_c + \tau/2]$ of length $\tau = 200\,\mu$s are collected whenever a threshold level of twice the standard deviation (2σ) is exceeded in a reference signal. The average of all subwindows in each signal reveals the evolution of the coherently coupled contribution. τ is chosen such that coherent structures can be well covered and related during and beyond their lifetime, and that correlations between the sample windows are avoided. The results do not change qualitatively with the choice of the threshold level.

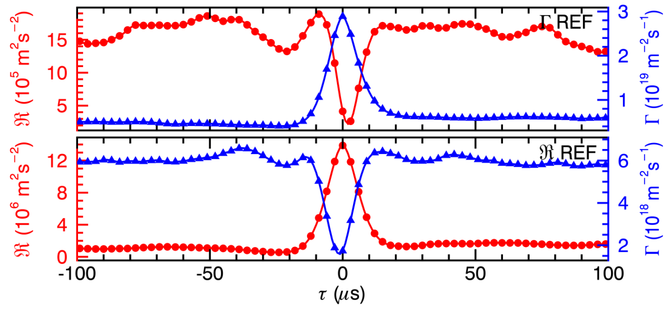

FIG. 3. Top: Conditionally averaged zonal Reynolds stress (●) triggered on events in net radial particle transport (▲). Bottom: Particle transport as triggered on Reynolds stress events. Uncertainties lie in the range of the symbol size.

An amount of $N \approx 2400-2500$ events is detected when conditionally sampling $\Re$ and Γ with respect to events in Γ and $\Re$, respectively, covering about 7% of the entire time series. In Fig. 3, the conditional averages are shown centered around the peak levels in the reference signal. Examining their dynamics reveals an almost constant ambient level in both Γ and $\Re$ embedding the coherent events of about 30 μs lifetime around the triggers. During the fivefold increase in particle transport, seen at the top of Fig. 3, the Reynolds stress decreases to about $1/10$ before it resets to its original value. Similarly, as the $\Re$ reference increases 10 times, Γ drops to $1/5$, as seen at the bottom of Fig. 3. A striking feature observed is a strong temporal anticorrelation between Γ and $\Re$, which were previously seen in Fig. 2 to peak in the same poloidal region. The observed dynamical interplay between Γ and $\Re$ aligns with the results in Ref. [12], where an increase in heating power triggers an L-H transition with increased $\Re$ and decreased turbulent transport.

V. DYNAMICAL DENSITY-POTENTIAL COUPLING AND SPECTRAL DECOMPOSITION

The anticorrelation of particle transport and Reynolds stress can be elucidated in terms of the dynamical evolution of the density-potential coupling. In this regard, the net particle transport is formally linked to the wave-number-integrated cross-power spectrum of spatial fluctuations in the density and potential [38]:

$$\Gamma = \frac{1}{B}\sum_k k\,A_{n\phi}(k)\sin\alpha_{n\phi}(k), \qquad (3)$$

with cross-amplitude ($A_{n\phi}$), and -phase ($\alpha_{n\phi}$) spectra. In particular, the direct dependence of Γ on ϕ results from the relation $\hat{v}_r \sim -ik_\theta\hat{\phi}$ between the Fourier components. From Eq. (3), it is clear that $\alpha_{n\phi} = 0$ is associated with no transport, which refers to an adiabatic $\tilde{n}$-$\tilde{\phi}$ coupling. Its deterioration is reflected in an increased phase shift with maximum contribution to transport for $\alpha_{n\phi} = \pi/2$. Adiabaticity, as shown in Ref. [14], is required for the Reynolds-stress mechanism. Nonetheless, the formal dependence of $\Re$ on the $\tilde{n}$-$\tilde{\phi}$ coupling is less clear than for Γ.

An appropriate, independent measure of the density-potential coupling for comparison with the temporal evolution of Γ and $\Re$ is provided by a cross-amplitude-weighted spectral

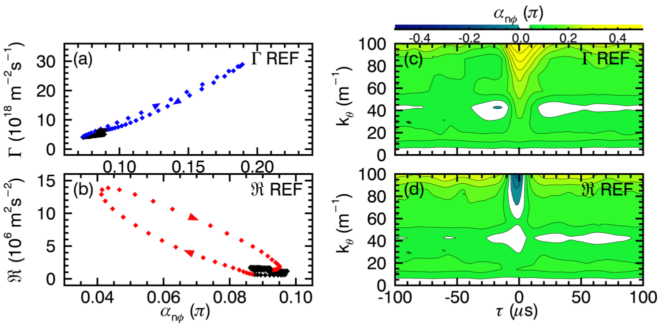

FIG. 4. (a) Turbulent particle transport and (b) Reynolds stress versus the $\tilde{n}$-$\tilde{\phi}$ phase shift during Γ and $\Re$ events, respectively. Colored points represent the state during the event, while black points show the ambient levels. Arrow heads indicate the temporal evolution. Evolution of the spectral density-potential cross-phase during Γ (c) Gamma; and (d) $\Re$ events.

phase according to Ref. [39]:

$$\alpha_{n\phi}(\tau) = \frac{\sum_k \alpha_{n\phi}(k,\tau) A_{n\phi}(k,\tau)}{\sum_k A_{n\phi}(k,\tau)}, \tag{4}$$

where the time dependence relative to the coherent trigger events is maintained via the conditional sampling technique. The amplitude weighting avoids the overestimation of low-power contributions.

Figure 4(a) and 4(b) show the dynamics of Γ and $\Re$ with respect to the evolution of the $\tilde{n}$-$\tilde{\phi}$ phase shift, according to Eq. (4) as obtained from conditional sampling within the time period τ. Before and after the events, the parameter $\alpha_{n\phi}$ resides closely fixed to values around $\approx 0.09\,\pi$, together with almost constant levels in both particle transport and Reynolds stress. During the events, a clear trend can be seen: $\alpha_{n\phi}$ varies dynamically, showing a clear correlation and anticorrelation with Γ and $\Re$, respectively, with values of 0.99 and -0.92. Γ peak events are associated with larger $\alpha_{n\phi}$ than $\Re$. Cross-trigger results (not shown) reveal a continuation of Γ and $\Re$ into the lower and higher $\alpha_{n\phi}$ range, respectively, reflecting the anticorrelation seen in Fig. 3.

The increase in Γ expected from the destabilization mechanism of drift waves is experimentally demonstrated here to be evolving with a dynamically varying $\tilde{n}$-$\tilde{\phi}$ phase shift. The dynamical relation between Γ and $\alpha_{n\phi}$ is consistent with the spatial dependence observed in Ref. [40]. In addition, the first direct experimental confirmation of the $\Re$ dependence on the $\tilde{n}$-$\tilde{\phi}$ coupling (represented by decreasing $\alpha_{n\phi}$), together with the inherent anticorrelation between net particle transport and Reynolds stress in toroidally confined plasmas, is presented as a logical consequence of the vortex tilting mechanism in drift-wave turbulence.

Figure 4(c) and 4(d) show the conditionally sampled spectral decomposition $\alpha_{n\phi}(k_\theta, \tau)$, revealing the dominantly involved scales in detail. Before and after the coherent events, the phase remains roughly constant. A striking increase and decrease of $\alpha_{n\phi}$ in the mid- and small-scale range around $60{-}100\,\mathrm{m}^{-1}$, corresponding to $k_\theta \rho_s > 0.6$, is observed to be coherently coupled to Γ and $\Re$, respectively, during their $30\,\mu\mathrm{s}$ lifetime. An instrumental influence can be ruled out as the cause of the effect since the evaluated signal-to-noise

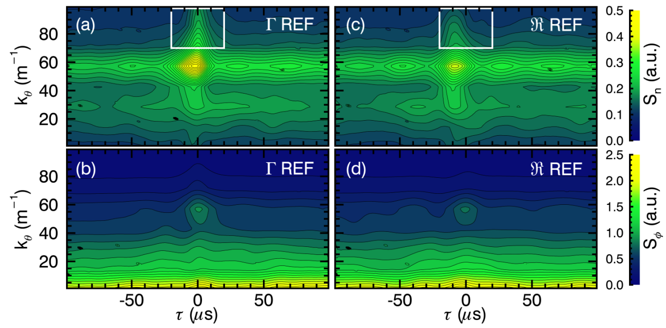

FIG. 5. Autopower spectrum of density (top) and potential fluctuations (bottom) during Γ (left) and $\Re$ events (right).

ratio of about 10^5 would introduce a maximum phase shift of only $0.002\,\pi$. Moreover, it can be clearly seen that, synchronously with the Reynolds stress, the cross-phase drops below zero within the dedicated wave-number range. According to Eq. 3, this scale range is thus associated with inward particle transport as attributed to drift-wave stabilization. The effect is limited to the poloidal region of elevated transport levels in Fig. 2(a). The formation of inward transport has been observed in tokamaks [41,42] and stellarators [43–45] under conditions of strong $E \times B$ shear. However, in the discharge presented here, strong shear is absent. The observed negative cross-phases can be understood as a fingerprint of the energy transfer established by the Reynolds stress, the analysis of which is beyond the scope of this work. The exclusivity of the scale range in which $\alpha_{n\phi}$ is changing indicates a prospective significance of the turbulence amplitudes on these scales for the formation of Γ and $\Re$, too.

From Eq. 4, it is evident that different scales contribute differently to the coupling according to the relative power contribution. The spectral dynamics in the individual fluctuation-power distributions, $S_n(k_\theta, \tau)$ and $S_\phi(k_\theta, \tau)$, during the reference events, is shown in Fig. 5. An effect in the form of increased fluctuation power is most distinct in the density around $k_\theta \approx 60\,\mathrm{m}^{-1}$. It occurs for both reference frames, with a slightly stronger effect and a distinct contribution at smaller scales for events in Γ than in $\Re$. Since the net particle transport is observed in Fig. 3 to drop in conjunction with the Reynolds stress and the fluctuation amplitudes are observed to increase in that time frame, the cross-phase is the only formal candidate making Γ drop. The exact role of the amplitudes for the anticorrelation can be examined in more detail on the basis of the cross-amplitude spectra, shown in Fig. 6. In both cases, increased contributions occur during the event at intermediate scales around $60\,\mathrm{m}^{-1}$, with a higher intensity and a distinct tail at smaller scales for Γ reference, coinciding with that of increased $\alpha_{n\phi}(k_\theta, \tau)$ in Fig. 4(c). It is seen clearly in Fig. 6(a) and 6(b) that both Γ and $\Re$ increase with the wave-number-averaged cross-amplitude levels, going along with correlation values of 0.94 and 0.84, respectively. In contrast to the cross-phase dependence in Fig. 4, the correlation with the cross-amplitude levels is now positive for both reference frames. Specifically, increased $\Re$ values go along with increased $A_{n\phi}$ levels while the cross-phase drops.

This is further substantiated when correlating cross-amplitude with the cross-phase, as shown in Fig. 7. The

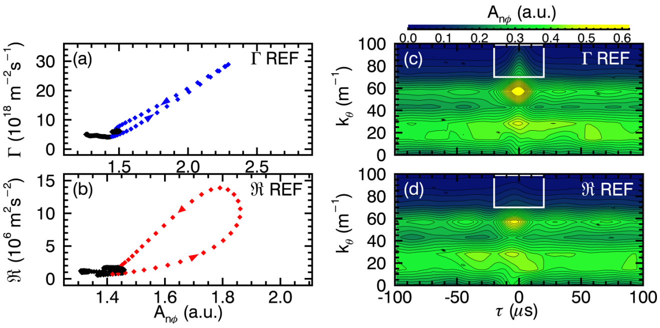

FIG. 6. Left: (a) Turbulent particle transport and (b) Reynolds stress versus average cross-amplitude during Γ and ℜ events, respectively (same representation as in Fig. 4). Right: The density-potential cross-amplitude evolution during (c) Γ and (d) ℜ events.

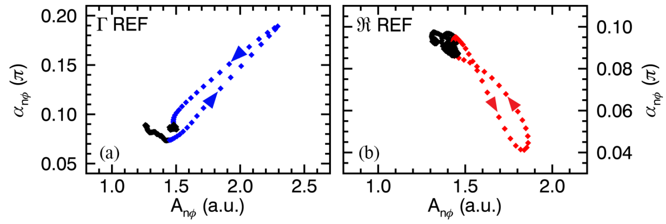

FIG. 7. Average cross-phase versus average cross-amplitude during Γ (a) and ℜ events (b) (similar representation as in Fig. 4).

positive correlation during Γ events is attributed to the destabilization of drift waves as perceived through the power contribution in $A_{n\phi}$ at wave numbers of $60 - 100\,\mathrm{m}^{-1}$, where the $\tilde{n}$-$\tilde{\phi}$ phase shift points to destabilizing polarization. During ℜ events, however, the correlation is negative. The small-scale contributions, which were observed in Fig. 6 to be characteristic of the destabilization during Γ events, are less prominent during ℜ events and are also associated with weaker and even negative cross-phases, that is, weaker destabilization and even stabilization. Hence, the absence of unstable small-scale contributions on average appears to limit the growth of fluctuation levels as well as destabilization at the expense of particle transport and in favor of Reynolds stress.

In fact, the increase in ℜ is not due to destabilization in the course of polarization: destabilization as indicated by $\alpha_{n\phi}$ was not observed to introduce $A_{v_r v_\theta}$ for ℜ. For Γ reference, $A_{v_r v_\theta}$ was roughly constant while for ℜ reference it actually decreased with increasing $\alpha_{n\phi}$. Hence, ℜ is correspondingly determined by the $v_r - v_\theta$ phase relation as governing the vortex tilt. The dominant role of the phase relation is consistent with the spatial representation given recently in Ref. [46].

Moreover, the disparity in the small-scale contributions during Γ and ℜ resembles a stronger weight of larger poloidal scales during ℜ, which is consistent with vortex tilting. This might lead to a change in the k_r/k_θ ratio toward larger weighting of the asymmetric geodesic curvature in linear drift-wave growth rates, leading to potentially stronger poloidal displacement of the Reynolds-stress distribution observed in Fig. 2(a).

VI. SUMMARY AND CONCLUSION

In summary, the dynamical interplay between turbulent particle transport and Reynolds stress was experimentally investigated using a poloidal multiprobe array at the stellarator TJ-K. While an adiabatic density-potential coupling with small $\tilde{n}$-$\tilde{\phi}$ cross-phases is expected to be essential for the Reynolds stress mechanism, Γ is associated with a deterioration of the coupling in the form of an increased cross-phase. Both Γ and ℜ were, for the first time, resolved simultaneously and related to a dynamically varying density-potential cross-phase to unravel their observed spatial coincidence under mutually exclusive $\tilde{n}$-$\tilde{\phi}$ coupling prerequisites. Net particle flux and Reynolds stress, as conditionally sampled with respect to each other, were observed to be temporally anticorrelated. Both were shown to evolve consistently with the cross-phase. An anticorrelation of ℜ with the cross-phase displays ℜ as a consequence of efficient vortex tilting in response to the distortion of density perturbations in drift-wave turbulence. A correlation of Γ with the cross-phase, on the other hand, reflects dynamically enhanced $E \times B$ particle flux through curvature-driven destabilization of drift waves. Small-scale contributions with $k_\theta \rho_s > 0.6$ were identified to be predominantly involved in this competitive process. Specifically, this range is found to regulate net particle transport through negative cross-phases, indicating spectral contributions of inward particle flux during Reynolds stress, which accounts for the anticorrelation in the dynamical stabilization-destabilization competition.

The presented findings emphasize the role of the dynamical interplay between plasma-density and -potential fluctuations in the regulation and spatial formation of turbulent transport and Reynolds stress. This sheds light on a potential interaction mechanism for the formation of transport barriers at the edge of fusion plasmas.

ACKNOWLEDGMENTS

This work has been funded by the Deutsche Forschungsgemeinschaft (DFG) under Grant No. 471314753.

[1] A. J. Wootton, B. A. Carreras, H. Matsumoto, K. McGuire, W. A. Peebles, C. P. Ritz, P. W. Terry, and S. J. Zweben, Phys. Fluids B **2**, 2879 (1990).

[2] F. Wagner, G. Becker, K. Behringer, D. Campbell, A. Eberhagen, W. Engelhardt, G. Fussmann, O. Gehre, J. Gernhardt, G. v. Gierke, G. Haas, M. Huang, F. Karger, M. Keilhacker, O. Klüber, M. Kornherr, K. Lackner, G. Lisitano, G. G. Lister, H. M. Mayer *et al.*, Phys. Rev. Lett. **49**, 1408 (1982).

[3] F. Wagner, G. Fussmann, T. Grave, M. Keilhacker, M. Kornherr, K. Lackner, K. McCormick, E. R. Müller, A. Stäbler, G. Becker, K. Bernhardi, U. Ditte, A. Eberhagen, O. Gehre, J. Gernhardt, G. v. Gierke, E. Glock, O. Gruber, G. Haas, M. Hesse *et al.*, Phys. Rev. Lett. **53**, 1453 (1984).

[4] P. H. Diamond and Y. Kim, Phys. Fluids B **3**, 1626 (1991).

[5] A. Fujisawa, K. Itoh, H. Iguchi, K. Matsuoka, S. Okamura, A. Shimizu, T. Minami, Y. Yoshimura, K. Nagaoka, C. Takahashi, M. Kojima, H. Nakano, S. Ohsima, S. Nishimura, M. Isobe, C.

Suzuki, T. Akiyama, K. Ida, K. Toi, and S.-I. Itoh, Phys. Rev. Lett. **93**, 165002 (2004).
[6] P. H. Diamond, S.-I. Itoh, K. Itoh, and T. S. Hahm, Plasma Phys. Controlled Fusion **47**, R35 (2005).
[7] T. Estrada, T. Happel, C. Hidalgo, E. Ascasíbar, and E. Blanco, Europhys. Lett. **92**, 35001 (2010).
[8] L. Schmitz, L. Zeng, T. L. Rhodes, J. C. Hillesheim, E. J. Doyle, R. J. Groebner, W. A. Peebles, K. H. Burrell, and G. Wang, Phys. Rev. Lett. **108**, 155002 (2012).
[9] I. Cziegler, A. E. Hubbard, J. W. Hughes, J. L. Terry, and G. R. Tynan, Phys. Rev. Lett. **118**, 105003 (2017).
[10] A. Hasegawa and M. Wakatani, Phys. Rev. Lett. **59**, 1581 (1987).
[11] P. Manz, M. Ramisch, and U. Stroth, Phys. Rev. Lett. **103**, 165004 (2009).
[12] Z. Yan, G. R. McKee, R. Fonck, P. Gohil, R. J. Groebner, and T. H. Osborne, Phys. Rev. Lett. **112**, 125002 (2014).
[13] I. Cziegler, G. Tynan, P. Diamond, A. Hubbard, J. Hughes, J. Irby, and J. Terry, Nucl. Fusion **55**, 083007 (2015).
[14] B. D. Scott, New J. Phys. **7**, 92 (2005).
[15] N. Fedorczak, P. Diamond, G. Tynan, and P. Manz, Nucl. Fusion **52**, 103013 (2012).
[16] B. Schmid, P. Manz, M. Ramisch, and U. Stroth, New J. Phys. **19**, 055003 (2017).
[17] P. Manz, A. Stegmeir, B. Schmid, T. T. Ribeiro, G. Birkenmeier, N. Fedorczak, S. Garland, K. Hallatschek, M. Ramisch, and B. D. Scott, Phys. Plasmas **25**, 072508 (2018).
[18] P. H. Diamond, Y.-M. Liang, B. A. Carreras, and P. W. Terry, Phys. Rev. Lett. **72**, 2565 (1994).
[19] P. Manz, M. Ramisch, and U. Stroth, Phys. Rev. E **82**, 056403 (2010).
[20] U. Stroth, P. Manz, and M. Ramisch, Plasma Phys. Controlled Fusion **53**, 024006 (2011).
[21] B. Schmid, P. Manz, M. Ramisch, and U. Stroth, Phys. Rev. Lett. **118**, 055001 (2017).
[22] A. Hasegawa and M. Wakatani, Phys. Rev. Lett. **50**, 682 (1983).
[23] M. Wakatani and A. Hasegawa, Phys. Fluids **27**, 611 (1984).
[24] S. J. Camargo, D. Biskamp, and B. D. Scott, Phys. Plasmas **2**, 48 (1995).
[25] J. M. Dewhurst, B. Hnat, and R. O. Dendy, Phys. Plasmas **16**, 072306 (2009).
[26] M. H. Nasim, T. Rafiq, and M. Persson, Plasma Phys. Controlled Fusion **46**, 193 (2004).
[27] S. Garland, P. Manz, and M. Ramisch, Phys. Plasmas **27**, 052304 (2020).
[28] G. Birkenmeier, M. Ramisch, P. Manz, B. Nold, and U. Stroth, Phys. Rev. Lett. **107**, 025001 (2011).
[29] B. Scott, Plasma Phys. Controlled Fusion **39**, 471 (1997).
[30] N. Krause, C. Lechte, J. Stöber, U. Stroth, E. Ascasibar, J. Alonso, and S. Niedner, Rev. Sci. Instrum. **73**, 3474 (2002).
[31] S. Enge, G. Birkenmeier, P. Manz, M. Ramisch, and U. Stroth, Phys. Rev. Lett. **105**, 175004 (2010).
[32] S. Niedner, B. D. Scott, and U. Stroth, Plasma Phys. Controlled Fusion **44**, 397 (2002).
[33] N. Mahdizadeh, F. Greiner, T. Happel, A. Kendl, M. Ramisch, B. D. Scott, and U. Stroth, Plasma Phys. Controlled Fusion **49**, 1005 (2007).
[34] C. Lechte, S. Niedner, and U. Stroth, New J. Phys. **4**, 34 (2002).
[35] U. Stroth, F. Greiner, C. Lechte, N. Mahdizadeh, K. Rahbarnia, and M. Ramisch, Phys. Plasmas **11**, 2558 (2004).
[36] N. Mahdizadeh, F. Greiner, M. Ramisch, U. Stroth, W. Guttenfelder, C. Lechte, and K. Rahbarnia, Plasma Phys. Controlled Fusion **47**, 569 (2005).
[37] T. Ullmann, B. Schmid, P. Manz, G. E. M. Tovar, and M. Ramisch, Phys. Plasmas **28**, 052502 (2021).
[38] E. Powers, Nucl. Fusion **14**, 749 (1974).
[39] M. J. Burin, G. R. Tynan, G. Y. Antar, N. A. Crocker, and C. Holland, Phys. Plasmas **12**, 052320 (2005).
[40] T. Kobayashi, K. Itoh, T. Ido, K. Kamiya, S.-I. Itoh, Y. Miura, Y. Nagashima, A. Fujisawa, S. Inagaki, and K. Ida, Sci. Rep. **7**, 14971 (2017).
[41] J. Boedo, D. Gray, P. Terry, S. Jachmich, G. Tynan, R. Conn, and T.-. Team, Nucl. Fusion **42**, 117 (2002).
[42] D. Kong, T. Lan, A. Liu, C. Yu, H. Zhao, H. Shen, L. Yan, J. Dong, M. Xu, K. Zhao, J. Cheng, X. Duan, Y. Liu, R. Chen, X. Sun, J. Xie, H. Li, W. Liu, and T. H.-A. Team, Nucl. Fusion **57**, 014005 (2016).
[43] M. G. Shats and D. L. Rudakov, Phys. Rev. Lett. **79**, 2690 (1997).
[44] M. G. Shats, K. Toi, K. Ohkuni, Y. Yoshimura, M. Osakabe, G. Matsunaga, M. Isobe, S. Nishimura, S. Okamura, K. Matsuoka, and (C. H. S. Group), Phys. Rev. Lett. **84**, 6042 (2000).
[45] M. Ramisch, F. Greiner, N. Mahdizadeh, K. Rahbarnia, and U. Stroth, Plasma Phys. Controlled Fusion **49**, 777 (2007).
[46] T. Long, P. H. Diamond, R. Hong, W. Tian, R. Ke, Y. Zhou, Z. Wang, L. Nie, M. Xu, Z. Wang, B. Li, G. Hao, J. Li, G. Xiao, Z. Shi, W. Chen, and W. Zhong, Rev. Mod. Plasma Phys. **9**, 7 (2025).